

Machine Learning Approaches to Solar-Flare Forecasting: Is Complex Better?

VARAD DESHMUKH ¹, SRINIVAS BASKAR,¹ ELIZABETH BRADLEY ^{1,2}, THOMAS BERGER ³ AND JAMES D. MEISS ⁴

¹*Department of Computer Science
University of Colorado Boulder
Boulder CO 80309-0430 USA*

²*The Santa Fe Institute
Sante Fe NM 87501 USA*

³*Space Weather Technology Research and Education Center
Boulder CO 80309-0429 USA*

⁴*Department of Applied Mathematics
University of Colorado Boulder
Boulder CO 80309-0526 USA*

ABSTRACT

Recently, there has been growing interest in the use of machine-learning methods for predicting solar flares. Initial efforts along these lines employed comparatively simple models, correlating features extracted from observations of sunspot active regions with known instances of flaring. Typically, these models have used physics-inspired features that have been carefully chosen by experts in order to capture the salient features of such magnetic field structures. Over time, the sophistication and complexity of the models involved has grown. However, there has been little evolution in the choice of feature sets, nor any systematic study of whether the additional model complexity is truly useful. Our goal is to address these issues. To that end, we compare the relative prediction performance of machine-learning-based, flare-forecasting models with varying degrees of complexity. We also revisit the feature set design, using topological data analysis to extract shape-based features from magnetic field images of the active regions. Using hyperparameter training for fair comparison of different machine-learning models across different feature sets, we show that simpler models with fewer free parameters *generally perform better than more-complicated models*, ie., powerful machinery does not necessarily guarantee better prediction performance. Secondly, we find that *abstract, shape-based features contain just as much useful information*, for the purposes of flare prediction, as the set of hand-crafted features developed by the solar-physics community over the years. Finally, we study the effects of dimensionality reduction, using principal component analysis, to show that streamlined feature sets, overall, perform just as well as the corresponding full-dimensional versions.

Keywords: solar flares — topological data analysis — machine learning

1. INTRODUCTION

Solar flares are produced as a result of intense release of magnetic energy from active regions on the surface of the Sun. The high-energy plasma emitted in conjunction with these eruptions can cause catastrophic events on Earth, with potentially trillions of dollars in associated economic losses. With enough notice, it is possible to mitigate some of the effects of these events, so forecasting is of obvious importance. In current operational practice, flare forecasts are produced by human experts using established classification systems (McIntosh 1990; Hale et al. 1919) to categorize active regions into various classes. A forecast is then constructed by consulting lookup tables of flaring rates for each category, which are derived from historical records (Crown 2012). Over the past two decades, there has been a great deal of effort devoted to machine learning (ML) solutions to this problem, as discussed below. After being trained on

corpora of observations of the Sun to learn correlations between the data and known instances of solar flares, these models can be applied to new observations to generate flaring forecasts.

The most commonly used observations in solar-flare forecasting are magnetic field images called *magnetograms* that are captured by the Helioseismic and Magnetic Imager (HMI) onboard the Solar Dynamics Observatory (SDO). The SDO, located in an inclined geosynchronous orbit around Earth, has been operational since 2010, recording the vector magnetic field data on the side of Sun’s photosphere that is visible from Earth. HMI supplies not only full-disk images of the Sun, but also cutouts of each active region as it moves across the photosphere, recorded at a cadence of 12 minutes. These cutouts are called *Spaceweather HMI Active Region Patches* or SHARPs. Each SHARPs record contains values for the radial, polar, and azimuthal components B_r , B_θ , and B_ϕ of the magnetic field at the location sampled by each pixel, along with a number of aggregate properties, such as the magnetic flux or the electric current. These physics-inspired attributes are carefully chosen by experts so as to be relevant to the flaring phenomenon.

This information has been used in different ways in a variety of machine-learning methods. Some researchers have trained models directly on the raw SHARPs images: e.g., (Huang et al. 2018; Park et al. 2018; Zheng et al. 2019; Li et al. 2020; Abed et al. 2021; Zheng et al. 2021). However, it is well known in the ML literature that “featurizing” data—preprocessing it to extract higher-level properties that are salient in a given context—can be extremely advantageous. The notion of salience is problem-specific; in computer vision, for instance, useful features might be edges or polygons. The attributes in the SHARPs metadata are a natural feature set for the flare forecasting problem, and most ML work to date has followed that reasoning. A wide range of models have been trained on this feature set: linear discriminant analysis (Leka & Barnes 2007), logistic regression (Yuan et al. 2010), LASSO regression (Campi et al. 2019), support vector machines (Bobra & Couvidat 2015), random forests or extremely randomized trees (Nishizuka et al. 2017; Campi et al. 2019)—and, in recent years, deep-learning models like multilayer perceptrons (Nishizuka et al. 2018), long short-term memories (Chen et al. 2019), and autoencoders (Chen et al. 2019).

The performance of these ever-more-complicated models, however, is no better than that of the human forecasters (Barnes et al. 2016; Leka et al. 2019a,b). Moreover, high model complexity may not actually be an advantage in this application. It is possible that this is due simply to data limitations: in general, more-complex machine-learning models require larger training sets to effectively extract the patterns needed for prediction. This issue is exacerbated when correlations are deeply embedded in complex data for complex situations. A second issue is the nature of the training data. Until very recently, ML-based flare forecasting work had not moved beyond the original SHARPs data: that is, the images themselves (i.e., the B values at each pixel) and the associated physics-based features. Choosing features that are scientifically meaningful makes good sense, of course, but ML methods can sometimes leverage attributes that are not obvious to human experts. For example, a recent *Nature* paper reports on using ML to discover a previously unknown correlation between geometric and topological attributes of knots (Davies et al. 2021). A third and related concern is the dimensionality of the training data. This, too, is a well known issue in the ML community, but there has been little exploration of this matter in the context of ML-based flare forecasting methods. Existing approaches have used the *complete* SHARPs feature set, but it may well be the case that a carefully crafted subset of these features would work as well—or perhaps even better.

In this paper, we aim to address the issues raised in the previous paragraph. Our first objective is to make a systematic, meaningful comparison of the predictive performance of machine-learning flare-forecasting models with varying complexity. The specific question we aim to address is: *How does increasing model complexity affect 24-hour forecast accuracy for solar flares?* To that end, we use four ML models: logistic regression, extremely randomized trees (ERTs), multilayer perceptrons (MLPs), and long short-term memories (LSTMs). Here, we define complexity informally as the number of parameters that are optimized during the training of the model. For example, logistic regression requires calculating a scaling weight for each feature involved, whereas MLPs and LSTMs are complex networks with hundreds of nonlinear, weighted connections that are adjusted during training. Comparing different ML models is not a trivial task, given the complexity of the training process. Each method has a number of free parameters, known as *hyperparameters*, that control the learning process: the learning rate in neural networks, for instance, or the maximum number of trees in an ERT. In order to make a systematic and fair comparison, we use an established hyperparameter tuning framework (Liaw et al. 2018) to optimize the performance of each model, then train it on a set of SHARPs from the period 2010-2017, each labeled as to whether that region produced a flare within the following 24 hours. Finally, we use various standard metrics to compare the predictive accuracy of these models on a different set of similarly labeled active regions. The results show that the simpler models (logistic regression and ERT) perform better than the more-complicated MLP and LSTM models.

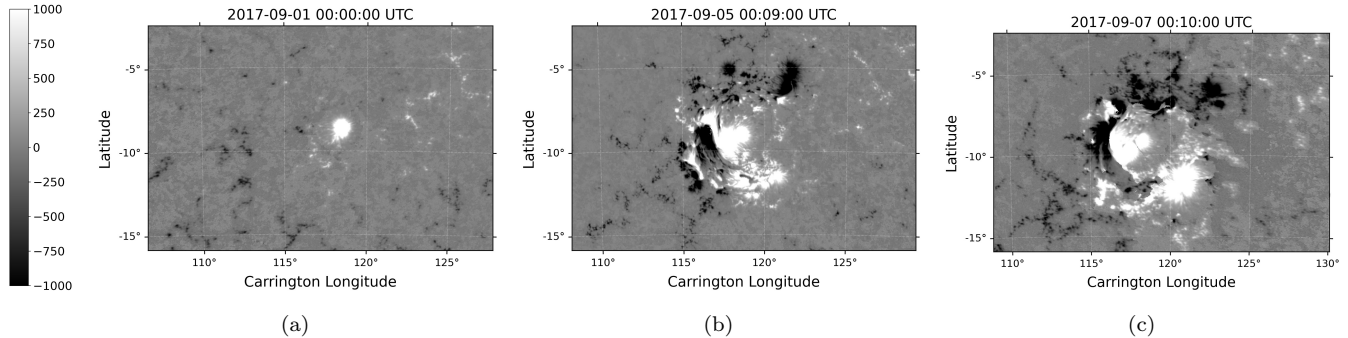


Figure 1. Radial component of magnetogram observations of sunspot #AR 12673, which produced M- and X-class flares during its journey across the solar disk in September 2017: (a) at 0000 UT on 9/1, (b) at 0900 UT on 9/5, approximately 24 hours before producing an X-class flare, and (c) at 1000 UT on 9/7, during an M-class flare.

The second objective of this paper is to explore *whether there are useful ways to move beyond the set of physics-based attributes in the SHARPs metadata*. Conjecturing that the shape of the magnetic structures in the photosphere could provide important clues about the evolving complexity of the field leading up to an eruption, we focus specifically on the abstract spatial properties of the magnetograms, such as the number of “holes” in a thresholded image of the magnetic field strength, extracted using topological data analysis. Our preliminary studies using multilayer perceptron models (Deshmukh et al. 2020, 2021a) suggested that features like this could perform as well as a basic set of SHARPs features. This was significant because the SHARPs feature set has been designed by experts, while the topological features are straightforward spatial attributes that require no hand crafting. However, that study used a single ML model and the comparison only involved a subset of the SHARPs features. In this paper, we perform a more-extensive comparison using the four ML models listed above and a more-comprehensive physics-based feature set. We also explore dimensionality reduction. Feature sets often contain correlations and redundancies: e.g., the mean and total values of some derived quantity. Removing these redundancies can both speed training and increase accuracy. Here, we use principal component analysis and find that models trained on the most significant principal components of each feature set¹ largely equaled the performance of those trained on the full set of features. This is an advantage since the amount of data required to successfully train a machine-learning model grows with its dimensionality.

The outline of this paper is as follows. Section 2 describes the details of the magnetogram data set and the labeling procedure. The different feature sets—SHARPs and topological—are discussed in Section 3. Section 4 describes the machine-learning models, the hyperparameter tuning framework, and the dimensional reduction strategy. The results are given in Section 5, and Section 6 concludes.

2. DATA

We use magnetic field images captured by the Helioseismic and Magnetic Imager (HMI) instrument onboard the Solar Dynamics Observatory for our study (Scherrer et al. 2012). This data set is available on the Stanford Joint Space Operations Center in the form of the Spaceweather HMI Active Region Patches mentioned in Section 1: rectangular cutouts of the photospheric vector magnetic fields. Here we use the `hmi.sharp_cea_720s` variant, which stores the Lambert Cylindrical Equal-Area projection of the magnetic field. Of the three field components in each SHARPs image, we use only the radial component, B_r . This is standard practice in ML-based flare forecasting work, as the radial surface field is used as the boundary condition for computing global coronal magnetic fields that are not yet routinely measurable (Caplan et al. 2021). Figure 1 shows a series of SHARPs observations of a single active region. In each panel, white represents the positive polarity of the radial flux, while black corresponds to negative polarity. Magnetic loops formed from emerging flux on the surface of the Sun manifest as pairs of dark and bright spots that represent their footpoints. Panel (a) shows the radial flux captured early in the evolution of the active region (AR) where the configuration is simple, with one positive and one negative footpoint corresponding to the ends of a single flux loop. Later, as shown in Fig. 1(b), the AR develops a complex pattern of positive and negative spots that exhibit

¹ those explaining 98.5% of the variance

shearing. This configuration indicates that the field lines in the chromosphere have become twisted, and this may lead to a build-up of magnetic energy, to magnetic reconnection, and to a solar eruption. Indeed, a high-intensity flare was generated in this active region 24 hours after the observation in panel (b). Panel (c) shows the radial post-flare flux, which is still complicated though perhaps less sheared than panel (b). This reduction in complexity is expected after the release of magnetic energy from the eruption.

For the study reported here, we choose SHARPs records from May 2010 to December 2017, using a one-hour cadence to reduce redundancy between consecutive images. This data set contains a total of 505,872 records. For training the ML models, each image is labeled based on whether the corresponding AR produced a flare in the next 24 hours. This information is not part of the HMI data set, so we use the NOAA Geostationary Operational Environment Satellite (GOES) X-ray Spectrometer flare catalog,² which contains records of the location, time, and magnitude of all solar flares since 1975. This catalog categorizes flares into five classes based on their intensity, from the weaker A, B and C, to the stronger M and X class flares. For our period, the GOES database reports 509 M-class flares and 36 X-class flares. Focusing on the stronger flares because of their potentially catastrophic consequences, we label each SHARP as flaring if an M1.0+ flare (one with an intensity above $10^{-5} \frac{W}{m^2}$) occurred from it within 24 hours after the observation time; otherwise, it is labeled as non-flaring. This yields a data set containing 3872 active regions, with 453,273 SHARPs labeled as non-flaring and 5769 as flaring. This kind of imbalance is a major issue from a machine-learning point of view, as we will discuss further below.

Training, optimizing and evaluating ML models requires splitting the data into training, validation and testing sets respectively. We assign all images of a given AR to a single set, rather than choosing the images for each set randomly. This ensures that observations of the same AR at different points in its evolution do not appear in both the training and testing sets, thus preventing a possible artificial score improvement from testing the model on data related to that used for training. Of the 3872 active regions, 70% were used for training (for fitting the model to the data), 10% for the validation (for selection of optimal hyperparameters), and 20% for the testing (to evaluate the trained and tuned models on previously unseen data). We produce ten different training-validation-testing splits through randomized selections, each generated with a different seed. These serve as ten trial runs of the experiment of training, optimizing, and testing our models.

3. FEATURIZATION OF MAGNETOGRAMS

The raw magnetogram data described in the previous section (e.g., the value of B_r at every pixel in a SHARPs record) can be used directly to train models like convolutional neural networks, which were developed for the specific purpose of learning patterns in images. Alternatively, the magnetogram data can be preprocessed to extract meaningful numerical attributes that can then be used to train other types of ML models, including support vector machines, extremely randomized trees, or logistic regression models. Feature engineering—the task of crafting a set of attributes that help the ML methods learn better—can be a real challenge. The more salient the features are in the context of the task at hand, the more traction they give the method, but it is not always obvious which attributes to choose. Domain knowledge can be useful in this endeavor, but unexpected attributes can also be predictive, particularly in the context of complicated problems and rich data.

Here, we work with two different feature sets: (i) a set of standardized physics-based properties used by many solar flare prediction methods and (ii) a set of abstract properties derived using an shape-based featurization method first proposed in (Deshmukh et al. 2020). In addition we also consider a third feature set that combines (i) and (ii).

3.1. *Physics-based features*

Each record in the SHARPs data set includes a set of metadata containing values for a variety of numerical attributes that represent properties of the corresponding active region. These attributes, developed and refined by the solar physics community over the past 11 years, are given in Table 1. They are predominantly derived from the raw magnetic flux observations and are believed to be useful indicators of solar flares. Their values are calculated automatically and stored by the Joint Space Operations Center group at Stanford.³ The vast majority of ML-based flare forecasting work has, as mentioned above, used these 20 quantities as the feature set.

3.2. *Shape-based features*

² www.ngdc.noaa.gov/stp/space-weather/solar-data/solar-features/solar-flares/x-rays/goes/xrs/

³ <http://jsoc.stanford.edu/>

Acronym	Description	Units
LAT.FWT	Latitude of the flux-weighted center of active pixels	<i>degrees</i>
LON.FWT	Longitude of the flux-weighted center of active pixels	<i>degrees</i>
AREA_ACR	Line-of-sight field active pixel area	<i>micro hemispheres</i>
USFLUX	Total unsigned flux	<i>Mx</i>
MEANGAM	Mean inclination angle, gamma	<i>degrees</i>
MEANGBT	Mean value of the total field gradient	<i>G/Mm</i>
MEANGBZ	Mean value of the vertical field gradient	<i>G/Mm</i>
MEANGBH	Mean value of the horizontal field gradient	<i>G/Mm</i>
MEANJZD	Mean vertical current density	<i>mA/m²</i>
TOTUSJZ	Total unsigned vertical current	<i>A</i>
MEANALP	Total twist parameter, alpha	<i>1/Mm</i>
MEANJZH	Mean current helicity	<i>G²/m</i>
TOTUSJH	Total unsigned current helicity	<i>G²/m</i>
ABSNJZH	Absolute value of the net current helicity	<i>G²/m</i>
SAVNCPP	Sum of the absolute value of the net currents per polarity	<i>A</i>
MEANPOT	Mean photospheric excess magnetic energy density	<i>ergs/cm³</i>
TOTPOT	Total photospheric magnetic energy density	<i>ergs/cm³</i>
MEANSHR	Mean shear angle (measured using B_{total})	<i>degrees</i>
SHRGT45	Percentage of pixels with a mean shear angle greater than 45 degrees	<i>percent</i>
R.VALUE	Sum of flux near polarity inversion line	<i>G</i>

Table 1. The SHARPs feature set. Values for these 20 features, together with error estimates, are available for each magnetogram in the SDO HMI database. Abbreviations: *A* and *mA* are Amperes and milli-Amperes, respectively; *Mm* is megameters, *G* is Gauss and *Mx* is Maxwells.

The evolution of the magnetic fields in the Sun during the lead-up to a solar flare manifests as an increase in the complexity of the structures on the magnetogram. This observation, which is visually obvious from the shapes of the regions in Fig. 1, plays a critical role in the qualitative classifications used in operational space-weather forecasts. The McIntosh classification system used at the NOAA Space Weather Prediction Center, for instance, is based on characteristics like the presence of umbras and penumbras. These spatial details are, however, largely absent from the definitions of the SHARPs features of Table 1, most of which are aggregate quantities such as means or totals. Thus it seems natural to explore whether features that characterize shape would be useful in ML-based flare forecasting methods—not only because this is what human forecasters use in their classifications, but also because AR shape in the photosphere has fundamental, meaningful connections to the coronal magnetic field physics leading up to an eruption.

Topology is the fundamental mathematics of shape: it distinguishes sets that cannot be deformed into one another by continuous transformations. Part of this shape classification—homology—corresponds to the number of connected components, 2D holes, 3D voids, etc., of a set. These numbers are known as the Betti numbers, $\beta_0, \beta_1, \beta_2, \dots$, where β_k is the number of k -dimensional “holes.” Topological data analysis (TDA), or computational topology, operationalizes this framework for situations where one has only finitely many samples of an object. One way to create a shape from finite data is to “fill in the gaps” between the samples by treating two points as connected if they lie within some distance ϵ of one other. Building an approximating object in this fashion, TDA computes the Betti numbers, then varies ϵ and repeats the process. The dependence of β_k on ϵ provides a rich morphological signature that captures the shape of an object at multiple resolutions. One can construct an even richer representation by tracking the ϵ value at which each feature is formed, and at which it is destroyed or merges with another. This results in a set of (*birth, death*) values of ϵ for each feature (component, 2D hole, 3D void, etc.). This methodology has proved to be quite powerful; it has been successfully applied to a range of different problems ranging from coverage of sensor networks (de Silva & Ghrist 2007), to structures in natural images (Ghrist 2008), neural spike train data (Singh et al. 2007), and even the large-scale structure of the universe (Xu et al. 2019).

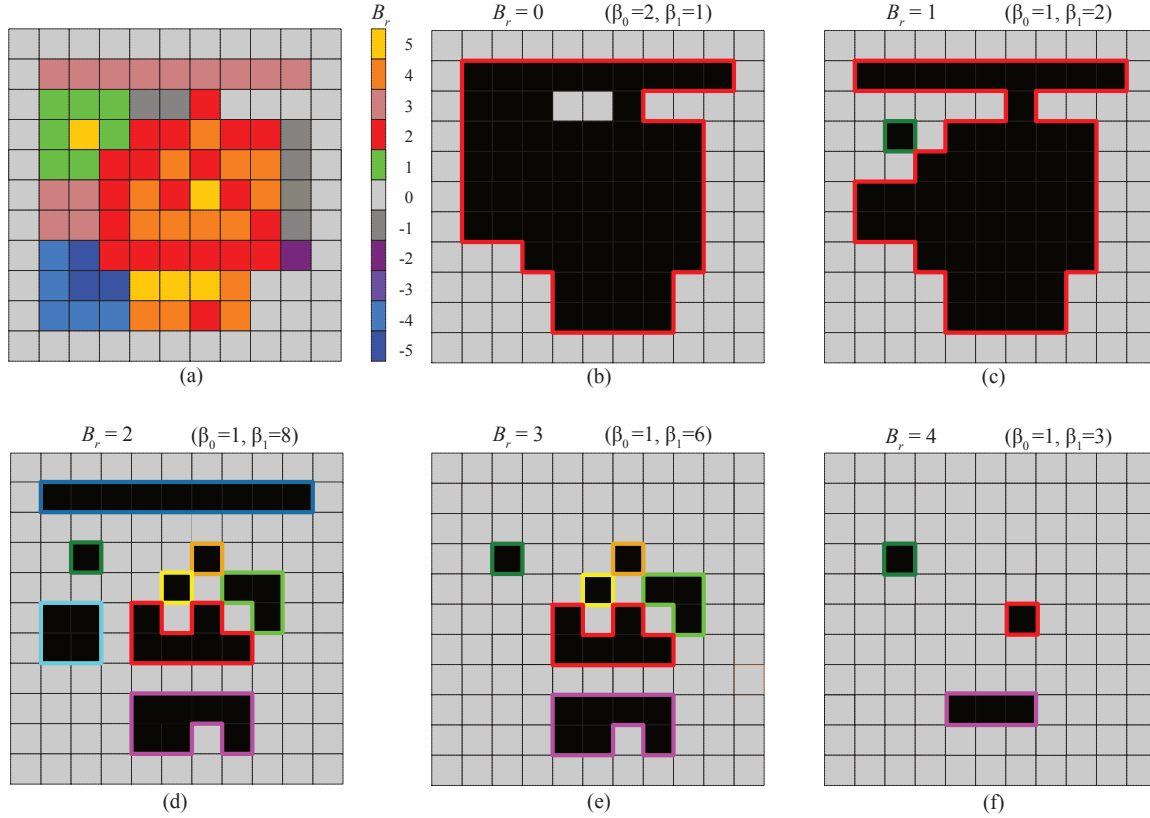


Figure 2. Topological data analysis for the example “image” in panel (a). The gray pixels in panels (b)-(f) represent the cubical complex of the image for five sub-level thresholding values, $B_r = 0, 1, 2, 3$, and 4. For each complex, the (β_0, β_1) values are given. The colored loops represent the holes in the thresholded images.

Our strategy for employing TDA in solar-flare forecasting, originally proposed in [Deshmukh et al. \(2020\)](#), is somewhat different from the approach described in the previous paragraph. Conjecturing that the shapes of the level sets of a magnetogram are of central importance in this problem, we use the magnetic field intensity B_r as the variable parameter, rather than a distance ϵ . We threshold the SHARPs image, keeping only the pixels where the magnetic field intensity falls at or below some value (i.e., sub-level thresholding) then compute the topology of the resulting object. By varying the threshold and tracking the birth and death of each feature, we obtain a signature that captures the morphological richness of a magnetogram in a manner that factors in the field strength as well as its spatial structure. A brief synopsis of this TDA-based feature extraction process follows; more details are given in [Deshmukh et al. \(2020\)](#).

We build what is technically known as a cubical complex ([Kaczynski et al. 2004](#)) from the pixels in the SHARPs image whose B_r values fall below some threshold. Pixels are connected in such a complex if they share an edge or a vertex. Since magnetograms are 2D images, only connected components and 2D holes (i.e., non-contractable loops) make sense—there is no higher-dimensional structure. Counting these gives β_0 and β_1 for the given threshold field, and this computation is then repeated for a range of B_r thresholds.

Figure 2 demonstrates this procedure for a simple example. Panel (a) represents an image, with each pixel colored according to intensity. Given an intensity value, a sub-level thresholded image corresponds to those pixels with a magnitude at or below the threshold. The gray regions in panels (b)-(f) represent such images for thresholds $B_r \in [0, 4]$. Pixels that share an edge or a vertex in a thresholded image become a component, which contributes to β_0 . Empty regions (black) in the interior of a thresholded image that are surrounded by a loop of connected gray pixels become holes, incrementing β_1 . In panel (b), where $B_r = 0$, the gray, thresholded image contains two components separated by the empty, black region where the intensity is larger than zero; thus $\beta_0 = 2$. There is a single non-contractable loop in the image (the red curve) that encloses the empty region, so $\beta_1 = 1$. Increasing the threshold to

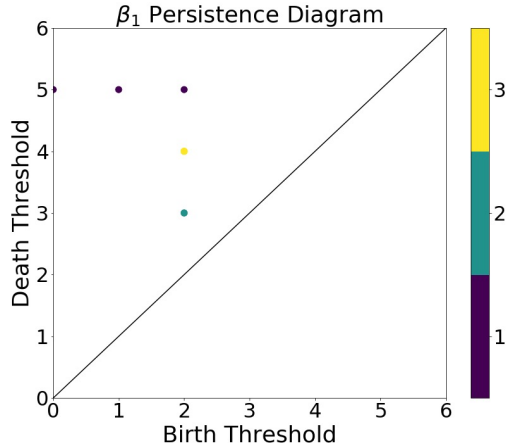


Figure 3. The β_1 persistence diagram for Fig. 2. The color scale represents the multiplicity, i.e., how many points share the same (*birth*, *death*) values.

$B_r = 1$, as in panel (c), causes the image to enlarge, shrinking the hole and splitting it into two; thus $\beta_1 = 2$.⁴ The two components from panel (b) merge in panel (c), and for the remainder of the thresholding process, the number of components remains one, so $\beta_0 = 1$. Upon raising the threshold, as shown in panel (d), the dominant hole splits into seven while the single-pixel hole remains intact, bringing the number of holes to eight ($\beta_1 = 8$). At $B_r = 3$ in panel (e), two holes disappear or “die”; thus $\beta_1 = 6$. Finally, for $B_r = 4$ in panel (f), the number of holes is reduced to three as three of the holes are filled in by new image pixels. If the threshold were raised to five (not shown), all pixels would be filled so that the image would have $\beta_0 = 1$ and $\beta_1 = 0$.

A number of different representations have been developed by the TDA community to capture the information about the scale and complexity of the different structures that is produced by such an analysis (Ghrist 2008). One of the most common, the persistence diagram (PD) (Edelsbrunner et al. 2000), is a plot of the birth and death values for each feature (e.g., the threshold value of B_r). Points that lie far from the diagonal on such a diagram are said to be *persistent*, as their birth and death values are widely separated. Points near the diagonal, which have short lifespans, are often formed due to noise in the data (Ghrist 2008). Figure 3 shows a β_1 PD for the example of Fig. 2. Each point in this PD corresponds to the (*birth*, *death*) thresholds for a hole in the filtered image. We use color to indicate the number of holes with same lifespan. In our example, there are three holes that live until $B_r = 5$. The longest-lived hole, indicated by the red border in Fig. 2, is born at $B_r = 0$, and thus corresponds to the point (0,5) on the PD. The single-pixel hole (green loop) is born at $B_r = 1$, giving the point (1,5) on the PD; the hole with the magenta border is born at $B_r = 2$ so it appears on the PD at (2,5). There are also five relatively short-lived holes; three of them (with yellow, orange and light-green borders) are represented by the yellow point (2,4) on the PD. The remaining two are the shortest-lived (cyan and blue) and correspond to (2,3).

One can similarly construct a β_0 persistence diagram to capture the birth and death of the connected components in the analysis. For the example here, this is not too interesting, since apart from the brief appearance of a second component at $B_r = 0$, there is only one component for all thresholds. This holds true for the β_0 PDs of actual magnetograms as well—they do not add much information to the analysis. For this reason, we restrict further analysis to β_1 PDs.

Persistence diagrams of real-world images can be far more complicated. Figure 4 shows β_1 PDs for the AR from Fig. 1. As in Fig. 2, these persistence diagrams show only the positive sub-level thresholds for B_r . The three images in Fig. 4 clearly bring out the evolving structure of this active region. The relatively simple structure of the fields in Fig. 1(a) creates one long-lived hole in Fig. 4(a) at approximately (0, 2600), corresponding to the central white spot, along with a large number of short-lived holes near the diagonal, which correspond to short-lived structures likely due to noise. The persistence diagram in panel (b), 24 hours before an X-class flare, has a large number of long-lived holes, reflecting the complexity of the structure of the active region at this time. After the flare, the PD in the rightmost

⁴ The green box corresponds to a loop in the image since gray pixels are connected at vertices.

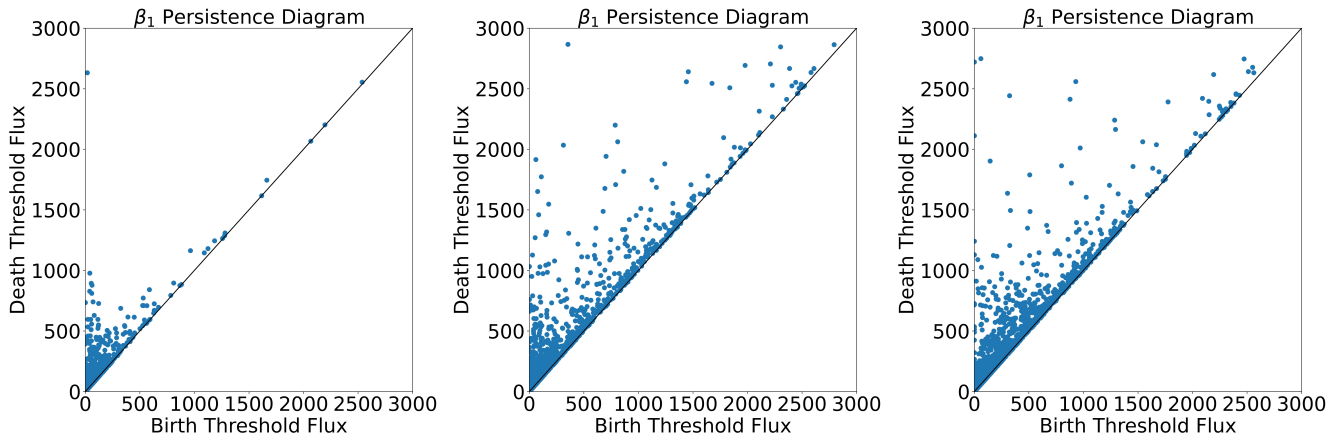


Figure 4. β_1 persistence diagrams generated from the positive magnetic flux density values of the magnetograms of Fig. 1. A clear change in the topology of the field structure is observed well in advance of the major flare eruption that occurred in this AR at 0910 UT on 6 September 2017.

panel is still complex, but the number of persistent holes has decreased; for example, the number of holes with a lifespan of 500 Gauss or more drops from 70 in panel (b) to 61 in panel (c).

We can also construct separate PDs for the negative flux regions by choosing negative threshold values, though in this case it is appropriate to use “super-level” instead of sub-level thresholding. Thus for this case we first include—for the threshold $B_r = 0$ —all pixels with $B_r \geq 0$, and then filter for increasingly negative values of B_r . For example, in Fig. 2(a), this process will leave a hole surrounding the blue pixels for a super-level threshold of $B_r = -3$. For the AR of Fig. 1, the resulting PDs (not shown) exhibit a similar evolution pattern to those in Fig. 4.

These results suggest that persistence diagrams can be useful indicators of impending solar flares. To operationalize this in the context of machine learning, however, there is an additional challenge. ML models generally require data that have a fixed dimension, but the PD contains an arbitrary number of $(birth, death)$ tuples. Various approaches to this “vectorization” problem have been proposed (Bubenik 2015; Adams et al. 2017; Chazal et al. 2014; Bubenik 2015; Reininghaus et al. 2015; Kusano et al. 2016; Carrière et al. 2017; Le & Yamada 2018; Carriere et al. 2020). Here we use a simple technique: we choose 10 equally spaced thresholds with $B_r > 0$ for sub-level thresholding and 10 thresholds with $B_r < 0$ for super-level thresholding, setting the maximum $|B_r| = 5000G$; this gives a range that covers the magnetic flux observed in most active regions.⁵ The spacing of the thresholds is chosen to ensure a good balance between redundancy (i.e., closely spaced, highly similar images with identical β counts) and adequate representation (avoiding a spacing so coarse as to miss important information). This process produces two 10×10 discrete PDs, one for positive and one for negative B_r . To telescope this information into a form that is usable by ML methods, we construct a 10-dimensional vector from each PD by simply counting the number of “live” holes at each threshold. These 20 values make up the feature set for the results presented in Section 5.

3.3. Feature-Set Reduction

As part of the training process, ML models learn which attributes of the input data, in which combinations, are meaningful. Their efficiency in doing so depends on the amount and complexity of the data, and also—importantly—on the way it is represented. In general, a larger feature set leads to increased model complexity, which in turn can result in overfitting and increased computational time (Goodfellow et al. 2016), as well as requiring larger training data sets. The nature of the individual features also matters. Features that are not salient, or that are redundant, slow down the learning process. For these reasons, it is important to minimize the number of features and maximize their relevance.

A good way to approach this problem is to apply dimensionality-reduction techniques to the feature space in order to find the most relevant subspaces. A variety of methods have been proposed for this, including principal component analysis, linear discriminant analysis, t-distributed stochastic neighbor embedding (Van der Maaten & Hinton 2008),

⁵ Specifically the thresholds are $\{263G, \dots, 4473G, 5000G\}$ for sub-levels and $\{-263G, \dots, -4473G, -5000G\}$ for super-levels.

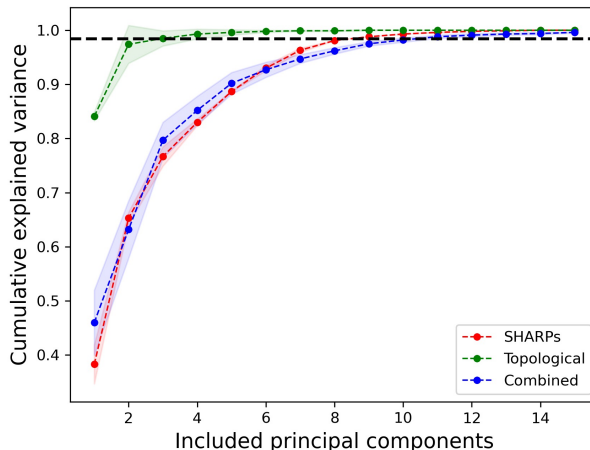
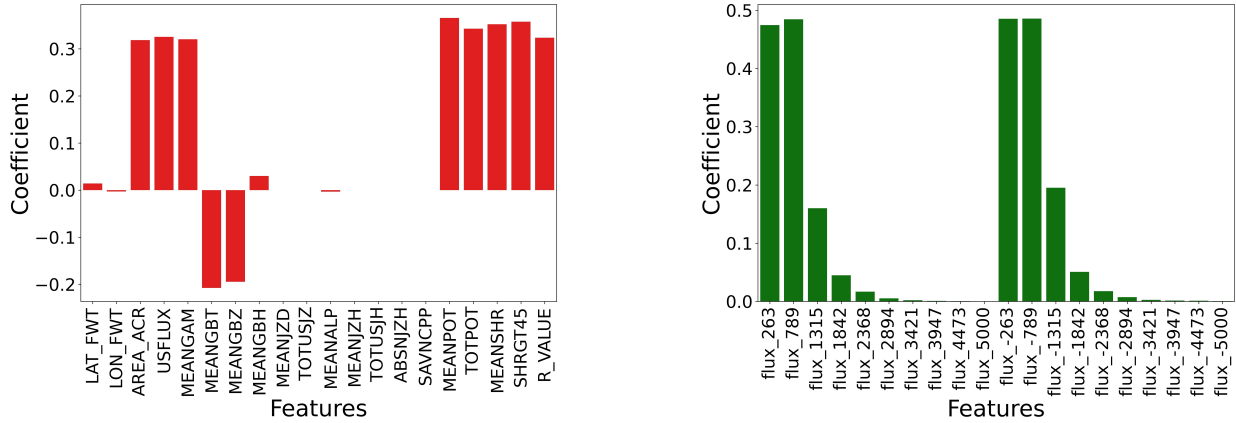


Figure 5. Cumulative explained variance plots of the principal components for the three feature sets, determined from the ten training sets. The darker curves represent the medians of the explained variance, while the shaded regions around them indicate standard deviations. The dashed line marks the 98.5% level.

uniform manifold approximation and projection (McInnes et al. 2018), etc. We use principal component analysis (PCA) because of its simplicity and effectiveness. It determines an alternative basis set to represent the data by iteratively constructing an orthogonal basis such that the variance of the data along the first dimension is maximal, the second dimension is in the direction of maximum variance that is orthogonal to the first dimension, and so on. One then typically keeps the first l , say, principal vectors that together account for some chosen fraction of the total variance. This approach, applied to an n -dimensional feature set, effectively reduces the dimensionality to l . Note that each of the l basis vectors may contain all of the original n values; we will discuss this more below.

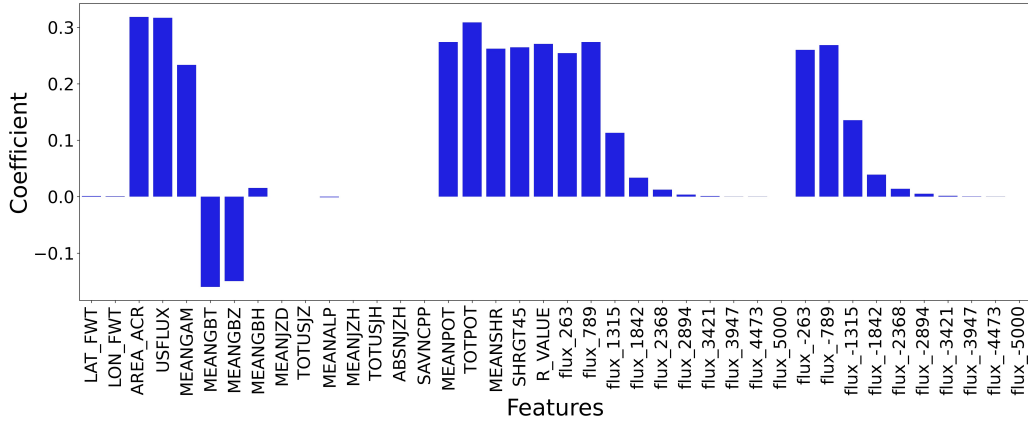
Applying this approach to the ten randomly shuffled training sets discussed in Sec. 2—first using the SHARPs feature set of Sec. 3.1, then the shape-based feature set of Sec. 3.2, and finally their combination—gives Fig. 5. For the SHARPs feature set, the first principal component captured 38% of the variance. As Fig. 5 shows, adding a second principal component increases the total to 60%. The topological feature set is much more anisotropic: its first principal component captures almost 85% of the variance of the data set, a level that requires four principal components in the SHARPs feature set. This is a direct reflection of the relevance of the TDA features for the purpose of flare prediction—as well as an indication of how many principal components will be needed as discriminating features for the corresponding ML models. To that end, we apply a threshold of 98.5% (the dashed line in Fig. 5) to select nine, three, and eleven dimensions from the orthogonal PCA representation for the reduced-dimension versions of the traditional, topological, and combined feature sets, respectively.

A detailed analysis of the reduced features is revealing. The coefficients of the first principal component—the weights of each SHARPs attribute in the basis vector—for one of the ten training sets are shown in Fig. 6(a). These results are to some extent consistent with the science: the `R.VALUE` and `USFLUX` attributes, which are known to be important for flare prediction, are weighted heavily in the first principal component of the SHARPs set. Note, though, that six other quantities are also weighted heavily in Fig. 6(a); moreover, this first principal component does not capture much of the variance, so one should not over-interpret its weights. Rather, one must think about *all* of the principal components for each feature set, acting together as a basis set for the new feature space. (A feature that is totally absent from every principal component, of course, is certainly not salient, but a low-weighted feature in the first one could have a high weight in another.) That being said, interpretation of Fig. 6(b) is somewhat different because, as Fig. 5 shows, the first principal component in the topological feature set captures a very large fraction of the variance. It is interesting to note that the topological features at lower magnetic fluxes are weighted more heavily in the first principal component, and with some $+/-$ symmetry. This makes sense in view of the nature of the threshold construction: a high threshold value removes much of the small-scale structure of the magnetogram, leaving only the highest-magnitude pixels. Finally, note that the first principal component from the combined feature set is a weighted combination of both SHARPs and TDA features. As we shall discuss in Section 5, this can have implications regarding model performance.



(a) SHARPs features set

(b) Topological feature set



(c) Combined feature set

Figure 6. The weights of the SHARPs, topological, and combined features in the first principal component of the corresponding feature set for one of the ten training sets examined in this paper. Labels of the topological features indicate the flux level of the threshold value used to construct those features.

Of course, PCA only finds a new basis set for the feature space; it does not produce a feature ranking. The previous paragraph only explains how one principal component is represented in terms of the original features, in one particular split of the data. Even though this gives possible ties to the physics, it does not represent a comprehensive, formal analysis of feature importance in the classification problem.

4. MACHINE LEARNING: MODELS AND FRAMEWORK

Evaluation and comparison of the predictive power of different machine-learning methods and different feature sets require care. The first step, as described at the end of Section 2, involves creating a *split* of the data set into training, validation, and test sets that are representative of the problem at hand, but do not artificially boost the performance of the model. Secondly, it is important to work with a *range* of ML models in order to be able to make general claims about whether one feature set is more useful than another. The models, as described in Section 4.1, were chosen to span ranges of complexity and strategies. Thirdly, ML methods have a number of *hyperparameters* that guide their training processes. Optimal values for these parameters depend on the model and the data, so a truly fair comparison requires

individualized tuning on a case-by-case basis. To that end, we use a k -fold cross-validation approach to automatically determine hyperparameters from the data as explained in Section 4.2. This systematic approach, which is in contrast to the trial-and-error approach used in the majority of the flare-prediction literature, ensures that each model achieves peak performance for each feature set.

4.1. Machine Learning Models

In our study, we use four different models: logistic regression, multilayer perceptrons, long short-term memories, and extremely randomized trees. In the following paragraphs, we give brief descriptions of these methods; for more details, please see [Murphy \(2012\)](#); [Goodfellow et al. \(2016\)](#) or any other basic machine-learning reference.

Logistic regression, perhaps the simplest of all models in the ML literature, uses a sigmoid function $h : \mathbb{R}^n \rightarrow [0, 1]$ as the basis function to the model the data:

$$h_{\theta}(x) = \frac{1}{1 + e^{-\theta^T x}}.$$

The vector θ corresponds to weights are applied to each element of the input vector x . In the context of the flare-prediction problem, $h_{\theta}(x)$ represents the flaring probability, which we then convert to a categorical “flare/no-flare” output using a threshold of 0.5—if $h_{\theta}(x) < 0.5$ then x is classified as non-flaring, otherwise it is classified as flaring. Training this model is a matter of determining values for θ ; we accomplish this using the LBFGS algorithm of ([Liu & Nocedal 1989](#)). The only hyperparameter involved in this process is the class weight that is used in the gradient descent: the higher the weight for one class, the more the model is penalized for getting the classification wrong.

A **multilayer perceptron** or MLP is a type of feedforward artificial neural network containing multiple layers of nodes or *neurons*, with the outputs of each layer propagated forward to the next layer. These canonical ML models contain an input layer, some number of hidden layers, and an output layer. The output of each neuron is a nonlinear function of its inputs with a single free parameter, typically a multiplicative constant, that is “learned” during training using some optimization strategy (e.g., gradient descent) on a suitable loss function: in this case, the weighted binary cross-entropy loss function, as described in [Deshmukh et al. \(2020\)](#). We employ the Adagrad optimizer ([Duchi et al. 2011](#)) to update the weights during gradient descent and an architecture with five dense layers containing 36, 24, 16, 8 and 2 nodes, respectively. This configuration was chosen using a manual trial-and-error approach. There are two important hyperparameters here: the class weight, which plays a similar role as in the logistic regression model, and the L2 regularization constant in the loss function, which ensures that none of the neuron weights becomes too large, which would lead to overfitting.

Active regions evolve over time in ways that are meaningful from the standpoint of solar physics. Logistic regression and MLPs cannot leverage the information that is implicit in a sequence of magnetograms, as their forecasts are based on individual snapshots. For that reason, a thorough evaluation of ML-based solar flare forecasting should include methods that factor in the history of the observations. To that end, we use **long short-term memories** (LSTMs), which are designed to work with temporal sequences of data, using a feedback loop in a hidden layer that takes the state calculated in time step t_{n-1} and feeds it to the same network for the sample at time step t_n . The LSTMs used in our study contain the same number of hidden layers as the MLP discussed above, but with such a feedback loop incorporated in one of the hidden layers. This strategy for propagating information forward in time is powerful, but it can complicate the training of these models. Simple gradient descent, for instance, can be problematic if there are long-term temporal dependencies in the data, since the gradient can decay as it is propagated through the time steps. To address this, LSTM nodes often incorporate mechanisms called “forget gates” that limit the number of steps through which information is propagated forward in time. This limit is an important choice, and one that is generally tuned by hand for a given model and data set. We use this approach and find that a sequence length of ten works well in our application. Like MLPs, LSTMs have two hyperparameters that significantly impact their performance: the weights in the binary cross-entropy loss function and the L2 regularization constant.

The fourth type of model used in our work is a type of Decision Tree, a class of ML models that have a tree-like structure, where each branch represents a decision based on some attribute of the data and the leaves correspond to the salient classes for the problem at hand (flaring and non-flaring, in our case). The input data dictate the path taken through the tree during the classification process, eventually routing the outcome to one of these classes. A major advantage of this strategy is that its results are an indication of how well each individual feature is able to divide the data set: a major step towards explainability, a critical challenge in modern AI. The main disadvantage of decision trees is their tendency for overfitting. One can mitigate this by building an ensemble of trees using a randomly chosen

subset of features at each branch point—a so-called “Random Forest”—and use the mean or mode of their predictions to classify a sample. The **extremely randomized tree (ERT)** (Geurts et al. 2006) that we use in this paper is a variant of this approach. These models have three hyperparameters: the class weight; the minimum impurity decrease, which controls when nodes will split; and the number of the trees in the ensemble, which mitigates overfitting.

This set of choices covers the full gamut of ML methods, in terms of architecture (e.g., tree-based or not) and complexity (number of free parameters), making it a sensible evaluation set.

4.2. Hyperparameter Tuning

Since the performance of an ML model depends on both the data and the training process, and because that training process is governed by the model’s hyperparameters, a fair comparison of two different ML models requires careful tuning of their hyperparameters. To do this, one evaluates its performance on a subset of the data, called the validation set, for different hyperparameter combinations. The best-performing combination is then used to train the model on the training set before it is evaluated on the corresponding test set. Using distinct subsets of the data for these three purposes ensures that the processes are completely independent.

Instead of using a single validation set, a better strategy is to perform what is called a k -fold cross-validation. In this approach, the training set is divided randomly into k subsets, or “folds,” of roughly equal size. For each evaluation of hyperparameters, one of the k folds acts as the validation set and the remaining $k - 1$ folds are merged to become the training set. After training, the model is then tested on the 1-fold validation set. This process is repeated using each of the k folds, individually, and the success of the hyperparameter combination is judged using the mean of the model’s performance metric across these runs.

This process is illustrated in Fig. 7. The first step is the standard random splitting of the data set, as described at

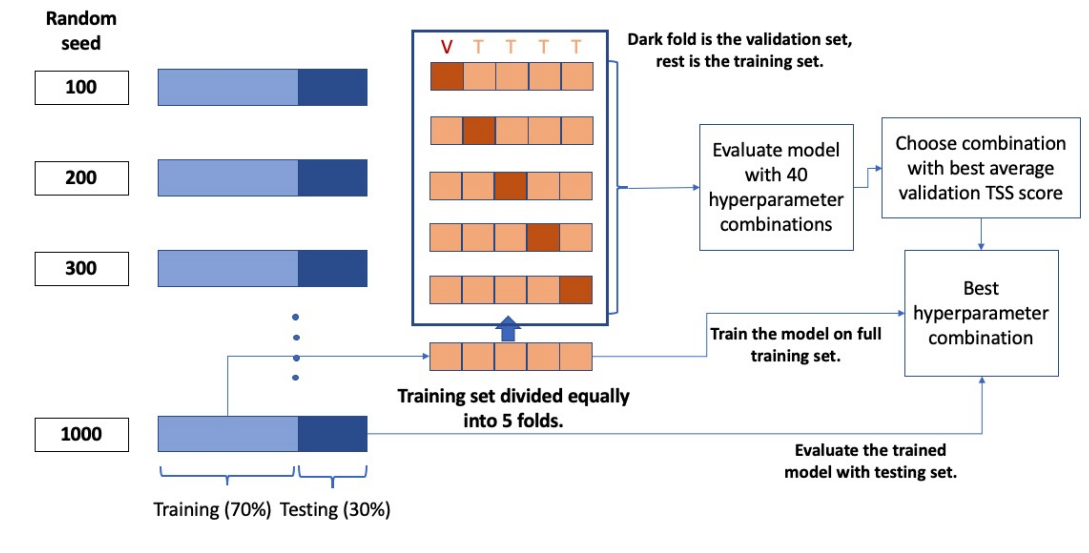


Figure 7. Hyperparameter tuning workflow.

the end of Section 2. We repeat this ten times using a 70%-30% ratio to generate ten trial runs, then generate k folds on each of those training sets. In machine-learning practice, k is generally chosen as 3, 5, or 10. In our case, $k = 5$ works well to produce sufficiently long training and validation sets. A second important decision in this tuning process is the sampling method for the hyperparameter value combinations. Various strategies have been proposed for this in the ML literature: grid search, random sampling, Bayesian sampling, etc. Here, we use the Bayesian optimization method of (Martinez-Cantin 2014), that uses Gaussian processes to mix exploration and exploitation in optimizing the hyperparameter combinations. We employ the Python implementation `BayesOptSearch` and use the `ray.tune` Python library (Liaw et al. 2018) to deploy the sampling and evaluation process on the graphics processing unit. As shown in Fig. 7, the `BayesOptSearch` method iteratively samples 40 hyperparameter combinations, choosing the one that gives

the best performance on the validation set, as measured by some metric that compares the forecast to the ground truth. (We use the true skill statistic, as described further in Section 5.) For `BayesOptSearch`, we use the upper confidence bound as the acquisition function, setting the exploration parameter $\kappa = 5$ in order to balance exploitation and exploration in the sampling process; see Snoek et al. (2012) for details. That sampling process begins with 10 uniformly chosen hyperparameter samples, continuing in steps of 10 to explore 40 hyperparameter combinations.⁶ The model is then trained on the full training set using the best-performing hyperparameter values before being evaluated on the 30% test set.

Not all hyperparameters require this kind of complex, computationally intensive treatment; some of them can be quite effectively tuned using manual trial-and-error. We employ a two-phase model-tuning strategy, first performing a hand optimization of hyperparameters such as the number of model layers, the nonlinear activation function, and the optimization function. These choices are made from among a finite set of options, and generally impact all metrics in a similar way. This is followed by the automated approach described above for tuning hyperparameters such as the loss function weights or the regularization penalty. Automatic tuning of these parameters is important for two reasons. Firstly, they take on continuous values, so hand-tuning becomes cumbersome. Secondly, their effects are not independent: changing one often improves one metric at the cost of another—a situation where an automated, systematic exploration of the search space can be especially appropriate. It is entirely possible, of course, to use the automated approach for *all* the hyperparameters, but that significantly increases the computation time.

Hyperparameter tuning is, as should be clear from the details above, a complex process. We offer these details here not only so that others can not only fully reproduce these results, but also use this framework in other applications that involve evaluation and comparison of flare-forecasting approaches. It is also worth mentioning that the metric that one uses to evaluate performance will affect the process, and in subtle ways: optimizing for pure accuracy, will produce different results than balancing false positives against false negatives. This matter is discussed further below.

5. RESULTS

In this section, we compare the relative prediction performance of the machine-learning based flare-forecasting models described in Section 4 for the three feature sets covered in Section 3. After extracting values for those features from the labeled data set described in Section 2, we carry out the hyperparameter tuning procedure outlined in the previous section on each model/feature-set combination, using the k -fold cross validation approach on the ten datasets, then train it with optimized hyperparameters on the corresponding training set. To evaluate the results, we run the model on the corresponding test set and compare its 24-hour forecasts to the ground truth using four standard prediction metrics: accuracy; the true skill statistic or TSS (also known as the $H\&KSS$), the Heidke skill score (HSS_2), frequency bias ($Bias$), and F_1 , which is the harmonic mean of precision and recall. These metrics, whose detailed formulae can be found in Barnes et al. (2016); Bobra & Couvidat (2015); Crown (2012), are derived from the entries of the contingency table—i.e., the numbers of true and false positives and true and false negatives. In the context of this problem, a flaring magnetogram (or more accurately, a magnetogram with an associated M1.0 or larger flare in the next 24 hours) is considered as a positive while a non-flaring magnetogram is considered a negative. Since our data set includes 5769 of the former and 447504 of the latter, accuracy is not a very useful metric here; a simple model that classified every input as non-flaring would be 98.7% accurate. The skill scores strike various balances between correctly forecasting the positive and negative samples. TSS ranges from $[-1, 1]$ and HSS_2 from $(-\infty, 1]$. In both cases, these scores are 1 when there are no false positives or false negatives, while a score of 0 means the model is doing only as well as a random forecast, essentially, an “always no-flare” forecast. $Bias$ has the range $[0, \infty]$, where $Bias < 1$ indicates under-forecasting (many false negatives), and $Bias > 1$ implies over-forecasting (many false positives). F_1 has the range $[0, 1]$ with 1 indicating a perfect forecast score. These metrics, all of which are used broadly in the flare-prediction literature, span the various methods used to quantify the performance of ML models.

As discussed in Section 4, hyperparameters for each model must be individually tuned in order to provide a fair comparison of their performance. The choice of metric plays a subtle role here, since hyperparameters can have different effects on the various metrics. Tuning performance based on values of one of them, then, can impact performance as measured by the others. The choice of metric is often left as a decision for the forecaster: some might wish to prioritize the TSS score, e.g. (Deshmukh et al. 2021a), while others might prefer a forecast that has lower false positive rate (Deshmukh et al. 2021b) or is more reliable (Nishizuka et al. 2021). In the problem treated here, where the data set is

⁶ i.e., using `initial_random_steps` in `ray.tune`, with `max_concurrent_trials=10`

ML Model	Feature Set	# of Parameters	Accuracy	TSS	HSS_2	F_1	$Bias$
Logistic Regression	SHARPs	21	0.87 ± 0.01	0.79 ± 0.01	0.13 ± 0.02	0.15 ± 0.02	11.44 ± 1.75
	Topological	21	0.87 ± 0.01	0.78 ± 0.02	0.12 ± 0.02	0.14 ± 0.02	11.88 ± 1.40
	Combined	41	0.87 ± 0.02	0.79 ± 0.02	0.13 ± 0.02	0.15 ± 0.02	11.76 ± 1.98
ERT	SHARPs	332	0.84 ± 0.01	0.79 ± 0.01	0.11 ± 0.01	0.13 ± 0.01	13.96 ± 0.81
	Topological	483	0.85 ± 0.02	0.76 ± 0.04	0.11 ± 0.02	0.13 ± 0.02	13.34 ± 1.93
	Combined	340	0.86 ± 0.02	0.77 ± 0.03	0.12 ± 0.02	0.14 ± 0.02	12.27 ± 2.12
MLP	SHARPs	2198	0.85 ± 0.02	0.76 ± 0.02	0.11 ± 0.02	0.13 ± 0.02	13.13 ± 2.42
	Topological	2198	0.85 ± 0.02	0.76 ± 0.02	0.11 ± 0.01	0.13 ± 0.01	13.56 ± 1.53
	Combined	2918	0.86 ± 0.03	0.76 ± 0.03	0.11 ± 0.02	0.13 ± 0.02	13.10 ± 1.78
LSTM	SHARPs	6662	0.87 ± 0.02	0.75 ± 0.02	0.12 ± 0.02	0.14 ± 0.02	11.90 ± 1.93
	Topological	6662	0.85 ± 0.02	0.75 ± 0.03	0.11 ± 0.02	0.13 ± 0.02	13.28 ± 2.11
	Combined	7382	0.86 ± 0.01	0.75 ± 0.02	0.12 ± 0.01	0.14 ± 0.01	12.00 ± 1.63

Table 2. 24-hour forecast performance of four machine-learning models using three feature sets. The third column shows the number of free parameters needed to classify a single data sample. For the ERT, this equals the average depth of the tree (the path taken by a data sample from the root to a leaf node in the tree).

highly imbalanced, an optimization based on accuracy would be a particularly bad choice, as it would lead to models defaulting to the “always no-flare” forecast. We use TSS in our work, choosing hyperparameters that maximize its values via the k -fold cross-validation described above. TSS is a common choice in the flare-forecasting literature, as well as the broader machine-learning literature. It does come with limitations, however: optimizing the TSS score can lead to high false positives, thereby impacting some of the other metrics like precision, F_1 , and $Bias$. This effect manifests in the results described below.

These experiments were carried out on an NVIDIA Titan RTX (24 GB, 33 MHz) GPU for the deep-learning models (MLP and LSTM), and on an Intel i9-9280X (3.30 GHz) CPU for the simpler models (logistic regression and ERT).⁷ Run times ranged from 2.5 seconds to train and 0.02 seconds to test each logistic regression model on the SHARPs feature set to 210 seconds and 9 seconds for the LSTM model using the combined feature set. The run time of the hyperparameter tuning procedure ranged from 40 seconds for each logistic regression model with the SHARPs feature set to just under two hours for each LSTM model with the combined feature set.

Table 2 compares the performance of the various models for the three feature sets: the traditional physics-based features that appear in the SHARPs metadata (Section 3.1), the shape-based attributes extracted from each magnetogram image using topological data analysis (Section 3.2), and a third set that combines the two. Note that the topological features perform just as well as the SHARPs features. Moreover, the combined feature set does not provide any improvement, confirming that neither feature set provides a significant advantage over the other. This is an answer to our second research question. Abstract spatial properties of active region magnetograms—calculated using abstract universal algorithms that quantify shape from raw image data without any assumptions about the underlying mechanics—appear to give ML methods just as much traction on flare-forecasting problems as the set of physics-based attributes that were hand-crafted by experts.

A between-model comparison addresses the first research question posed in Section 1: whether model complexity is an advantage in the context of this problem. The table suggests that the answer is no. Indeed, the general trend in the TSS scores shows that increased complexity slightly *reduces* performance. Indeed, even though the MLP and LSTM models have orders of magnitude more parameters, the simpler logistic regression and ERT models perform marginally better, as judged by the TSS scores. (For the other metrics, there is no significant variation among the four models.) This may simply be due to data limitations; recall that the higher the complexity of a machine-learning model, the more data is needed for training. If the training set is too small, the model will overfit that data, causing it to fail to generalize well to the testing set. Simpler models avoid this trap. Note that while ≈ 460000 samples might seem large, many of the images in the solar flare data set are similar, and almost all are non-flaring. In other words, the total amount of *information*—i.e., the number of sufficiently diverse and useful samples—is small in this data set.

⁷ Different machine-learning models lend themselves to different types of hardware, depending on how well they parallelize. The machine used to carry out these experiments affects only the run time, not the results.

Forecasting Window	Accuracy	TSS	HSS_2	F_1	$Bias$
24 hours	0.87 ± 0.01	0.79 ± 0.01	0.13 ± 0.02	0.15 ± 0.02	11.44 ± 1.75
12 hours	0.89 ± 0.02	0.82 ± 0.01	0.10 ± 0.03	0.11 ± 0.03	17.13 ± 4.10
6 hours	0.91 ± 0.01	0.82 ± 0.02	0.07 ± 0.02	0.07 ± 0.02	25.17 ± 4.83
3 hours	0.93 ± 0.01	0.79 ± 0.05	0.05 ± 0.01	0.05 ± 0.01	33.18 ± 4.60

Table 3. Logistic regression forecasts for different horizons.

Determining whether data limitations are in play is an important open problem in current ML research. One way to approach it is to compare the values of the weighted binary cross-entropy loss function across the models; another is to observe the patterns in the convergence over the training process. Both are problematic for the more-complex models in our study. The ERT model does not generate a loss, nor does it have an iterative training process. For models that do have an iterative training procedure (MLP and LSTM), we carried out the second test, and found that both the validation and training losses reached asymptotes during the training process, suggesting—but of course not proving—that overfitting is not at issue. The first approach is not useful in the case of the LSTM because one-to-one loss comparisons are problematic in such models due to the variation in the number of samples in the training and testing sets that occurs when the original data are converted to temporal sequences by the feedback loop in the model. In the future, as more data is recorded by SDO/HMI, we hope to learn, by re-running these experiments on longer, richer data sets, whether the effects described in this paragraph are artifacts of data limitations or something more fundamental.

To assess the effects of the prediction horizon, we carried out a set of experiments using the best-performing model/feature combination from Table 2 (logistic regression with the combined feature set) and generated forecasts for 3, 6, and 12 hours in addition to our previous 24 hour case. The results are shown in Table 3. As one would expect, the shorter the forecast window, the higher the accuracy, but the story for the other metrics is more complicated: TSS is roughly similar for all forecasting windows, while HSS_2 , F_1 , and $Bias$ actually *worsen* as the forecast window shrinks. This counterintuitive result is almost certainly due to the increasing fraction of negative samples: for each flare, fewer magnetograms will be labeled as “flaring within m hours” if m is smaller. This is, again, a side effect of tuning on the TSS score, as discussed above: its optimization leads to a high false positive rate for a severely imbalanced dataset.

The LSTM is not only the most complicated model in this study—by a factor of three, as judged by the number of free parameters—but also the only one that uses the AR *history*. In view of this, its lack of performance is particularly striking. The feedback loop in this architecture makes it difficult to deconvolve the effects of the temporal history and the number of parameters, so we cannot say for sure whether or not the former, alone, confers any advantage. Nevertheless, the additional free parameters certainly do not appear to help.

Our final research question concerned reduction of the dimension of the feature sets. To explore this, we re-process the data sets to calculate values for the PCA-based features detailed in Section 3.3, using 9, 3, and 11 PCA vectors for the traditional, topological and combined feature sets, respectively. We then re-tune the model hyperparameters and repeat the train/test procedure. The results are shown in Fig. 8. For all three feature sets, the performance of the full and reduced-order models are similar for the logistic regression, MLP, and LSTM models, as judged by TSS scores. This extends to the other metrics as well (not shown). In other words, we can successfully simplify these ML models by reducing the number of features *without sacrificing performance*. In view of the discussion above about data limitations, this is an obvious advantage, as models that work with smaller feature sets have fewer free parameters that must be learned from the same training data.

The ERT model, however, departs from this pattern, demonstrating a marked reduction in TSS scores for the PCA-reduced feature set. This effect is strongest for the topological feature set, followed by the SHARPs feature set, with the combined feature set seeing the smallest impact. A possible explanation for this performance degradation lies in the way ERTs are constructed. In a k -feature ERT, \sqrt{k} randomly chosen features are typically used to determine the split at each branch point. A reduction in the number of features, then, confines the exploration of the ERT parameter space. This could result in branches that do not effectively separate the positive and negative samples, thereby impacting the model performance. Modifying the training process to use all k features for choosing the best split can ameliorate this problem. Indeed after doing this, we find that there is no statistically significant difference between the reduced and the full feature sets for the TSS scores of the topological and combined feature sets. However, the SHARPs feature set does not show a similar improvement upon increasing the number of features used in the split. This disparity

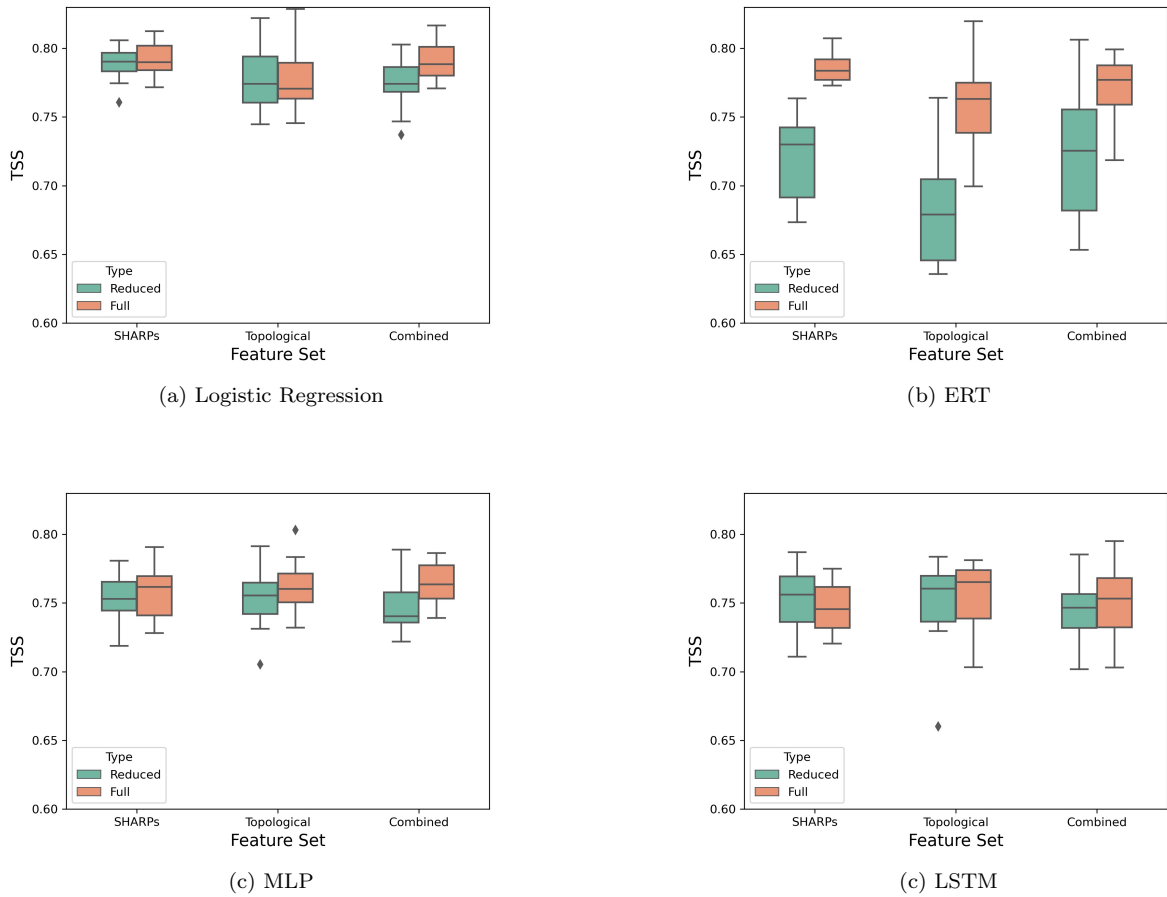


Figure 8. TSS score comparison in the form of box-whiskers plots for four ML models, trained on the three feature sets and their PCA reduced counterparts over ten trials. The central line each box represents the median TSS score while the top and bottom edge of the boxes represent the 25 and 75 percentiles over the ten trials. The whiskers on either sides are the upper and lower bounds for the scores in each experiment, and the dots represent the outliers (see the plotting manual <https://seaborn.pydata.org/generated/seaborn.boxplot.html> for the definition of outliers). After PCA reduction, the SHARPs feature set is reduced from 20 to 9 features, the topological set from 20 to 3 features, and the combined set from 40 to 11 features. For all models except for the ERT, the reduced feature set does just as well as the complete feature set.

suggests that the presence of shape-based features in the combined set helps make up for the shortcomings of the physics-based features. This agrees with the results in Section 3.3 that show both SHARPs and topological features are highly weighted in the first principal component of the combined feature set.

6. CONCLUSIONS

Machine learning-based solar flare prediction has been a topic of interest to the space weather community for some time. Various machine-learning models, ranging from simple tools like logistic regression to incredibly complex “deep-learning” models such as multi-layer perceptrons (MLPs) and long short-term memories (LSTMs), have been used to map the correlation between physics-based magnetic field features and the flaring probability in the near future. There have been studies that compared different machine-learning flare-forecasting models (Barnes et al. 2016; Nishizuka et al. 2017; Florios et al. 2018); however, the dominant focus of these papers has been on performance comparison and they only used the basic SHARPs feature set. Furthermore, none of these approaches performed a systematic, automated hyperparameter tuning process to assure a fair comparison, and only Florios et al. (2018) did any hyperparameter tuning at all (using a grid search method on discrete hand-selected values).

Our first objective in this paper was to systematically compare a set of machine-learning models and determine whether higher complexity is correlated with better performance. Using an automated hyperparameter tuning ap-

proach, we compared four models with increasing complexity: logistic regression, extremely randomized trees, MLP and LSTM. Across multiple experiments, and using an automated hyperparameter tuning approach, we showed that increasing the complexity of the model did not improve the model performance for the 24-hour M1.0+ flare-forecasting problem. (Note that we do not include convolutional neural networks as part of this study due to their high computational needs. However, we do address them separately in [Deshmukh et al. \(2021b\)](#).)

Secondly, we evaluated a new shape-based feature set that was introduced in [Deshmukh et al. \(2020\)](#) composed of quantities extracted from magnetograms using topological data analysis. The results from these features are compared to the standard physics-based SHARPs feature set. Our results extend previous pilot studies ([Deshmukh et al. 2020, 2021a](#); [Knyazeva et al. 2017](#)) by using a far more comprehensive SHARPs feature set, employing four different ML models, and using a systematic hyperparameter tuning methodology to ensure fairness in comparison. This broader and deeper study confirmed that the shape-based features—calculated using abstract and universal algorithms without any assumptions about the underlying physics—provide as much traction to ML models as the set of physics-based attributes that were hand-crafted by experts. Further, the combination of the shape-based and physics-based feature sets does not provide any improvement over the individual sets, confirming that neither feature set provides a significant advantage over the other.

Lastly, we studied a different aspect of model complexity: the dimensionality of the feature set. Using principal component analysis (PCA) to find relevant subspaces of the feature space, we studied the effect of dimensionality on model performance. We found that the topological feature set afforded the largest dimensionality reduction, and that the PCA-reduced datasets performed just as well as the original feature sets for three of the four ML models.⁸ In a data-limited situation, this is a major advantage for the effectiveness of machine-learning based solar-flare prediction methods, since more-complex models generally require larger training sets.

ACKNOWLEDGMENTS

This study was funded by a grant from the National Science Foundation (Grant No. AGS 2001670) and by a grant from the NASA Space Weather Science Applications Program (Grant No. 80NSSC20K1404).

⁸ The exception, the ERT model, did not improve due to architectural design choices.

REFERENCES

- Abed, A. K., Qahwaji, R., & Abed, A. 2021, *Advances in Space Research*, 67, 2544,
doi: <https://doi.org/10.1016/j.asr.2021.01.042>
- Adams, H., et al. 2017, *J. Mach. Learn. Res.*, 18, 218–252,
doi: [10.5555/3122009.3122017](https://doi.org/10.5555/3122009.3122017)
- Barnes, G., et al. 2016, *Astrophysical Journal*, 829, 89,
doi: [10.3847/0004-637X/829/2/89](https://doi.org/10.3847/0004-637X/829/2/89)
- Bobra, M. G., & Couvidat, S. 2015, *Astrophysical Journal*, 798, 135
- Bubenik, P. 2015, *J. Mach. Learn. Res.*, 16, 77–102,
doi: [10.5555/2789272.2789275](https://doi.org/10.5555/2789272.2789275)
- Campi, C., et al. 2019, *Astrophysical Journal*, 883, 150,
doi: [10.3847/1538-4357/ab3c26](https://doi.org/10.3847/1538-4357/ab3c26)
- Caplan, R. M., Downs, C., Linker, J. A., & Mikic, Z. 2021, *The Astrophysical Journal*, 915, 44,
doi: [10.3847/1538-4357/abfd2f](https://doi.org/10.3847/1538-4357/abfd2f)
- Carriere, M., Chazal, F., Ike, Y., et al. 2020, in *Proceedings of Machine Learning Research*, Vol. 108, *Proceedings of the Twenty Third International Conference on Artificial Intelligence and Statistics*, ed. S. Chiappa & R. Calandra (PMLR), 2786–2796.
<https://proceedings.mlr.press/v108/carriere20a.html>
- Carrière, M., Cuturi, M., & Oudot, S. 2017, in *Proceedings of Machine Learning Research*, Vol. 70, *Proceedings of the 34th International Conference on Machine Learning*, ed. D. Precup & Y. W. Teh (PMLR), 664–673.
<https://proceedings.mlr.press/v70/carriere17a.html>
- Chazal, F., Fasy, B. T., Lecci, F., Rinaldo, A., & Wasserman, L. 2014, in *Proceedings of the Thirtieth Annual Symposium on Computational Geometry*, SOCG'14 (New York, NY, USA: ACM), 474:474–474:483,
doi: [10.1145/2582112.2582128](https://doi.org/10.1145/2582112.2582128)
- Chen, Y., et al. 2019, *Space Weather*, 17, 1404,
doi: [10.1029/2019SW002214](https://doi.org/10.1029/2019SW002214)
- Crown, M. D. 2012, *Space Weather*, 10,
doi: [10.1029/2011SW000760](https://doi.org/10.1029/2011SW000760)
- Davies, A., Velickovic, P., Buesing, L., et al. 2021, *Nature*, 600, 70. <https://doi.org/10.1038/s41586-021-04086-x>
- de Silva, V., & Ghrist, R. 2007, *Algebr. Geom. Topol.*, 7, 339, doi: [10.2140/agt.2007.7.339](https://doi.org/10.2140/agt.2007.7.339)
- Deshmukh, V., Berger, T., Bradley, E., & Meiss, J. 2020, *Journal of Space Weather and Space Climate*, 10, 13,
doi: [10.1051/swsc/2020014](https://doi.org/10.1051/swsc/2020014)
- Deshmukh, V., Berger, T., Meiss, J. D., & Bradley, E. 2021a, in *Thirty-Fifth AAAI Conference on Artificial Intelligence*, AAAI 2021, *Thirty-Third Conference on Innovative Applications of Artificial Intelligence*, IAAI 2021, *The Eleventh Symposium on Educational Advances in Artificial Intelligence*, EAAI 2021, Virtual Event, February 2-9, 2021 (AAAI Press), 15293–15300.
<https://ojs.aaai.org/index.php/AAAI/article/view/17795>
- Deshmukh, V., Flyer, N., Sande, K. V. D., & Berger, T. 2021b, *Decreasing False Alarm Rates in ML-based Solar Flare Prediction using SDO/HMI Data*.
<https://arxiv.org/abs/2111.10704>
- Duchi, J., Hazan, E., & Singer, Y. 2011, *J. Mach. Learn. Res.*, 12, 2121–2159, doi: [10.5555/1953048.2021068](https://doi.org/10.5555/1953048.2021068)
- Edelsbrunner, H., Letscher, D., & Zomorodian, A. 2000, in *Proceedings 41st annual symposium on foundations of computer science*, IEEE, 454–463
- Florios, K., et al. 2018, *Solar Physics*, 293, 28,
doi: [10.1007/s11207-018-1250-4](https://doi.org/10.1007/s11207-018-1250-4)
- Geurts, P., Ernst, D., & Wehenkel, L. 2006, *Machine Learning*, 63, 3, doi: [10.1007/s10994-006-6226-1](https://doi.org/10.1007/s10994-006-6226-1)
- Ghrist, R. 2008, *Bulletin of the American Mathematical Society*, 45, 61, doi: [10.1090/S0273-0979-07-01191-3](https://doi.org/10.1090/S0273-0979-07-01191-3)
- Goodfellow, I., Bengio, Y., & Courville, A. 2016, *Deep Learning* (The MIT Press), doi: [10.5555/3086952](https://doi.org/10.5555/3086952)
- Hale, G. E., et al. 1919, *The Astrophysical Journal*, 49, 153,
doi: [10.1086/142452](https://doi.org/10.1086/142452)
- Huang, X., Wang, H., Xu, L., et al. 2018, *The Astrophysical Journal*, 856, 7, doi: [10.3847/1538-4357/aaae00](https://doi.org/10.3847/1538-4357/aaae00)
- Kaczynski, T., Mischaikow, K., & Mrozek, M. 2004, *Appl. Math. Sci.*, Vol. 157, *Computational Homology* (New York: Springer-Verlag)
- Knyazeva, I. S., Urtiev, F. A., & Makarenko, N. G. 2017, *Geomagnetism and Aeronomy*, 57, 1086,
doi: [10.1134/S0016793217080126](https://doi.org/10.1134/S0016793217080126)
- Kusano, G., Hiraoka, Y., & Fukumizu, K. 2016, 48, 2004.
<https://proceedings.mlr.press/v48/kusano16.html>
- Le, T., & Yamada, M. 2018, 31.
<https://proceedings.neurips.cc/paper/2018/file/959ab9a0695c467e7caf75431a872e5c-Paper.pdf>
- Leka, K. D., & Barnes, G. 2007, *Astrophysical Journal*, 656, 1173, doi: [10.1086/510282](https://doi.org/10.1086/510282)
- Leka, K. D., et al. 2019a, *Astrophysical Journal*, 243, 36,
doi: [10.3847/1538-4365/ab2e12](https://doi.org/10.3847/1538-4365/ab2e12)
- . 2019b, *Astrophysical Journal*, 881, 101,
doi: [10.3847/1538-4357/ab2e11](https://doi.org/10.3847/1538-4357/ab2e11)
- Li, X., Zheng, Y., Wang, X., & Wang, L. 2020, *The Astrophysical Journal*, 891, 10,
doi: [10.3847/1538-4357/ab6d04](https://doi.org/10.3847/1538-4357/ab6d04)

- Liaw, R., Liang, E., Nishihara, R., et al. 2018, arXiv preprint arXiv:1807.05118
- Liu, D. C., & Nocedal, J. 1989, *Mathematical Programming*, 45, 503, doi: [10.1007/BF01589116](https://doi.org/10.1007/BF01589116)
- Martinez-Cantin, R. 2014, *J. Mach. Learn. Res.*, 15, 3735–3739, doi: [10.5555/2627435.2750364](https://doi.org/10.5555/2627435.2750364)
- McInnes, L., Healy, J., Saul, N., & Großberger, L. 2018, *Journal of Open Source Software*, 3, 861, doi: [10.21105/joss.00861](https://doi.org/10.21105/joss.00861)
- McIntosh, P. S. 1990, *Solar Physics*, 125, 251, doi: [10.1007/BF00158405](https://doi.org/10.1007/BF00158405)
- Murphy, K. P. 2012, *Machine Learning: A Probabilistic Perspective* (The MIT Press)
- Nishizuka, N., Kubo, Y., Sugiura, K., Den, M., & Ishii, M. 2021, *Earth, Planets and Space*, 73, 1, doi: [10.1186/s40623-021-01381-9](https://doi.org/10.1186/s40623-021-01381-9)
- Nishizuka, N., et al. 2017, *Astrophysical Journal*, 835, 156, doi: [10.3847/1538-4357/835/2/156](https://doi.org/10.3847/1538-4357/835/2/156)
- Nishizuka, N., et al. 2018, *Astrophysical Journal*, 858, 113, doi: [10.3847/1538-4357/aab9a7](https://doi.org/10.3847/1538-4357/aab9a7)
- Park, E., Moon, Y.-J., Shin, S., et al. 2018, *The Astrophysical Journal*, 869, 91, doi: [10.3847/1538-4357/aaed40](https://doi.org/10.3847/1538-4357/aaed40)
- Reininghaus, J., Huber, S., Bauer, U., & Kwitt, R. 2015, in *2015 IEEE Conference on Computer Vision and Pattern Recognition (CVPR)*, 4741–4748, doi: [10.1109/CVPR.2015.7299106](https://doi.org/10.1109/CVPR.2015.7299106)
- Scherrer, P. H., Schou, J., Bush, R. I., et al. 2012, *Solar Physics*, 275, 207, doi: [10.1007/s11207-011-9834-2](https://doi.org/10.1007/s11207-011-9834-2)
- Singh, G., Memoli, F., & Carlsson, G. 2007, in *Eurographics Symposium on Point-Based Graphics*, ed. M. Botsch, R. Pajarola, B. Chen, & M. Zwicker (The Eurographics Association), doi: [10.2312/SPBG/SPBG07/091-100](https://doi.org/10.2312/SPBG/SPBG07/091-100)
- Snoek, J., Larochelle, H., & Adams, R. P. 2012, in *Advances in Neural Information Processing Systems*, ed. F. Pereira, C. J. C. Burges, L. Bottou, & K. Q. Weinberger, Vol. 25 (Curran Associates, Inc.). <https://proceedings.neurips.cc/paper/2012/file/05311655a15b75fab86956663e1819cd-Paper.pdf>
- Van der Maaten, L., & Hinton, G. 2008, *Journal of machine learning research*, 9
- Xu, X., Cisewski-Kehe, J., Green, S. B., & Nagai, D. 2019, *Astron. Comput.*, 27, 34, doi: [10.1016/j.ascom.2019.02.003](https://doi.org/10.1016/j.ascom.2019.02.003)
- Yuan, Y., et al. 2010, *Proceedings of the International Astronomical Union*, 6, 446 , doi: [10.1017/S1743921311015742](https://doi.org/10.1017/S1743921311015742)
- Zheng, Y., Li, X., Si, Y., Qin, W., & Tian, H. 2021, *Monthly Notices of the Royal Astronomical Society*, 507, 3519, doi: [10.1093/mnras/stab2132](https://doi.org/10.1093/mnras/stab2132)
- Zheng, Y., Li, X., & Wang, X. 2019, *The Astrophysical Journal*, 885, 73, doi: [10.3847/1538-4357/ab46bd](https://doi.org/10.3847/1538-4357/ab46bd)